Surface Corrected Lunar MTF Measurements in MODIS and VIIRS Using the SP Model

Truman Wilson and Xiaoxiong Xiong

***Abstract*—Lunar observations have been used for sensor performance assessments for a number of Earth-observing instruments, including the Moderate Resolution Imaging Spectroradiometer (MODIS) on board Terra and Aqua and the Visible Infrared Imaging Radiometer Suite (VIIRS) on board Suomi-NPP (SNPP) and NOAA-20 (N20). While the primary purpose of lunar observations in MODIS and VIIRS is radiometric calibration, these observations have been leveraged for other sensor performance assessments such as spatial registration and deriving the modulation transfer function (MTF). In this work, we will derive the lunar MTF using a knife edge approach similar to previous work. However, to further isolate the edge of the lunar disk when deriving the edge spread function (ESF), we will apply a lunar surface variation correction using a model based on data obtained by the Spectral Profiler (SP) on board the SELENE spacecraft. This model was provided to us by AIST in Japan. To align the measured and modeled data, we developed techniques for projecting the measured lunar surface pixels onto the radiance maps produced by the SP model. We correct the lunar surface variation while preserving the signal of the lunar disk edge in the ESF, and then calculate the MTF results using standard techniques. These results are in good agreement with previously published results from both Moon-based observations in MODIS and VIIRS and from the spectroradiometric calibration assembly (SRCA) on MODIS. With the exception of MODIS bands 1 and 2, the MTF is stable on orbit for the reflective bands in both instruments.**

***Index Terms*—MODIS, VIIRS, Spectral Profiler, lunar calibration, MTF, ESF**

I. Introduction

FOR Earth-observing satellite instruments, on-orbit calibration and characterization has been a key component of the long-term success of many missions. For the Moderate Resolution Imaging Spectroradiometer (MODIS, onboard Terra and Aqua) and the Visible Infrared Imaging Radiometer Suite (VIIRS, onboard Suomi-NPP (SNPP) and NOAA-20 (N20)), the on-orbit calibration is performed using a combination of internal and external calibration references [1]–[4]. The primary calibration methodology uses on-board calibrators (OBC) such as solar diffusers (SD) for the reflective solar bands (RSB) and blackbody (BB) targets for the thermal emissive bands (TEB). To supplement these calibrations, Earth-view (EV) observations have also been used over select sites due to their relatively stable reflectance properties [5], [6]. These EV targets can be seen by multiple instruments, sometimes in a near simultaneous observations, providing opportunities for instrument intercomparison [7]. Also, in-situ measurements are available for direct comparison at some locations [8]. In addition to EV measurements, both MODIS and VIIRS also use regularly scheduled spacecraft roll maneuvers in order to observe the Moon through their respective space-view (SV) ports [9]–[12]. The Moon has long been used as an external calibration target for satellite sensors due to its very stable reflectance over the lifetime of satellite missions.

While radiometric calibration has been the primary motivation for observing the Moon for MODIS and VIIRS, the Moon is also used for several other specialized characterization measurements. For whiskbroom sensors like MODIS and VIIRS, the Moon will appear at a different location in the image based on the spectral band's position on the focal plane assembly (FPA). Since the Moon is a well-resolved source against a dark background, it is a good target for spatial registration measurements, such as band-to-band registration (BBR) and detector-to-detector registration (DDR), as the Moon can be easily located in each band's image [13]–[17]. In addition to measurements of the bands spatial offsets, the Moon can also be used to measure the modulation transfer function (MTF) on orbit, which characterizes the system's spatial frequency response [16], [18], [19]. These on orbit measurements have been beneficial for determining whether the optical performance of long-term satellite missions changes over time. The lunar limb's sharp contrast with the dark background of space resembles a "knife edge", with the Moon's curvature and motion across the FPA allowing for sub-pixel sampling of the edge position. This technique has been described in detail in the literature and our implementation of it will be described in Section III [20]. Lunar "knife edge" measurements have been performed in the past for geostationary satellite instruments, such as the GOES-9 Imager, the Advanced Himawari Imager (AHI) on Himawari-8, and the Advanced Baseline Imager (ABI) on-board GOES-16/17 and for polar orbiting instruments like MODIS and VIIRS [16], [18]–[23].

While the lunar knife edge technique has been used effectively for MTF calculations, there have been issues with handling the variable surface reflectance of the Moon. Since the Moon's surface is non-uniform, undesirable frequency components can be introduced to the MTF from surface variation since the edge-spread function (ESF) does not come up to a constant value like a laboratory knife edge measurement. Various techniques have been implemented in order to mitigate this effect. A widely used technique is a masking and padding approach, where data that is a certain threshold away from the detected edge position is masked out and replaced with

T. Wilson is with Science Systems and Applications, Inc., Lanham, MD 20706 USA (e-mail: truman.wilson@ssaihq.com).

X. Xiong is with the Science and Exploration Directorate, NASA Goddard Space Flight Center, Greenbelt, MD 20771 USA (e-mail: xiaoxiong.xiong-1@nasa.gov).

constant values to simulate a flat lunar surface [19]–[21]. These values can be then be padded out away from the edge in order to increase the resolution of the fast Fourier transform (FFT) calculation used to compute the MTF. However, there can be difficulties when using this technique near locations with high surface variation at the edge of the Moon's disk in a waning phase [22].

In recent years, Caron *et al.* implemented a lunar surface variation correction to the ESF for MTF calculations in images from geostationary satellites using a lunar albedo map from NASA's Clementine mission [23]. The albedo map generated by Clementine covered the entire lunar surface at high resolution. By aligning the image position and rotation of the Clementine map with their measured images, the ESF could be appropriately corrected for surface variation effects and provide better consistency in the MTF results across multiple events. This technique was implemented for AHI on Himawari-8 and ABI on both GOES-16/17 with good results, which all view the Moon at higher resolution compared to instruments such as MODIS and VIIRS, which are the subject of this work. For low resolution images, new challenges arise when creating the model images that are used to produce the correction. In this work, we will show a new pixel mapping method that can be used to calculate each pixel of the model image by aggregating the model data over the pixel's field of view (FOV) on the lunar surface.

The Clementine data used by Caron *et al.* is effectively centered at 750-nm and requires an empirical gamma correction in order to apply it to the ABI bands, which range in wavelength from 0.47 to 2.2 μm. For this work, we opt instead to use a lunar reflectance model developed by Kouyama *et al.* using data from the Spectral Profiler (SP) on board the SELENE spacecraft, known as the SP Model [24]. The SP Model is able to generate simulated lunar images across 160 spectral channels ranging in wavelength from 0.51 to 1.64 μm. The output has a resolution of 0.5° in both selenographic latitude and longitude. This model also accounts for both the observer and solar positions allowing us to create predicted images tailored to each instrument and observation. While the wavelength range does not cover all of the MODIS or VIIRS RSB, it does cover bands at all of the available resolutions on both instruments. This will allow us to assess effectiveness of using a surface flattening correction on relatively low resolution images, which can be as low as 7 pixels wide for the full lunar disk for the MODIS 1-km bands.

The goals of this work can be divided into two main objectives: developing methodology for projecting the SP model output onto the measured imagery from MODIS and VIIRS, and deriving the MTF for select bands from Aqua and Terra MODIS and SNPP and N20 VIIRS. We will also show that using a surface correction for lunar images can be effective at relatively low resolution compared to previous work. In Section II, we will present the details of the instrument operation for both MODIS and VIIRS, specifically the image acquisition systems and lunar observations. In Section III, we will introduce the SP model and the methodology that we developed for mapping the SP model output onto the measured imagery. This methodology will allow us to implement a surface variation correction to the ESF and assess the effectiveness of such a correction on relatively low resolution images of the Moon. We will also show our derivation of the MTF from lunar images, which is similar to the lunar knife edge approach developed previously after the surface correction. Next, in Section IV, we will use the corrected images to derive the MTF for select bands from Aqua and Terra MODIS and SNPP and N20 VIIRS, and assess the stability of the MTF on-orbit. We will also compare these results to previous work, including the results as measured by the spectroradiometric calibration assembly (SRCA) on board the MODIS instrument. Finally, in Section V, we will present our conclusions.

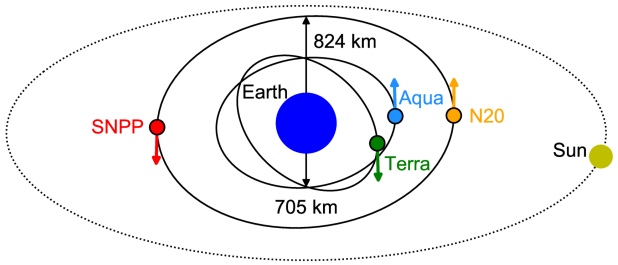

Fig. 1. A diagram of the relative orbits of the Terra, Aqua, SNPP, and N20 platforms (not to scale).

II. MODIS and VIIRS Instrument Operation

Both the MODIS and VIIRS instruments are whiskbroom scanning radiometers, which use rotating optical systems in order to acquire wide image swaths of EV scenes in the cross-track (scan) direction as the instrument orbits. Each satellite is in a polar orbit, with Terra in a descending daytime orbit with a 10:30 local equatorial crossing time and Aqua, SNPP, and N20 in ascending daytime orbits with a 13:30 local equatorial crossing time, as seen in Figure 1. For image acquisition, MODIS uses a double-sided scan mirror in order to direct light towards a set of 4 focal plane assemblies (FPA) [1]. For VIIRS, the scan mirror is replaced by a rotating telescope assembly (RTA) along with a double-sided half-angle mirror (HAM). VIIRS has 3 FPAs [2]. For both instruments, the FPAs divide the bands by wavelength, with the infrared bands being on separate, cooled FPAs, which are kept at temperatures below 85 K. Both instruments also use linear arrays of detectors, which construct 2D images through timed sampling of the detectors as the image moves across each FPA. MODIS has bands at 3 nadir spatial resolutions, with bands 1 and 2 at 250 m (40 detectors), bands 3-7 at 500 m (20 detectors), and bands 8-36 at 1 km (10 detectors). VIIRS has bands at 2 nadir spatial resolutions, the imagery bands, or I-bands (I1-I5), at 375 m (32 detectors) and the moderate resolution bands, or M-bands (M1-M16), at 750 m (16 detectors). VIIRS also contains a panchromatic day/night band (DNB), which aggregates the pixels of a charge-coupled device sensor to produce imagery at 750 m on ground throughout the scan.

The satellites carrying MODIS and VIIRS rotate in such a way to keep the instrument pointed towards nadir throughout the orbit. We can define the instrument coordinate system, or ICS, in the following way. We start with the instrument z-axis

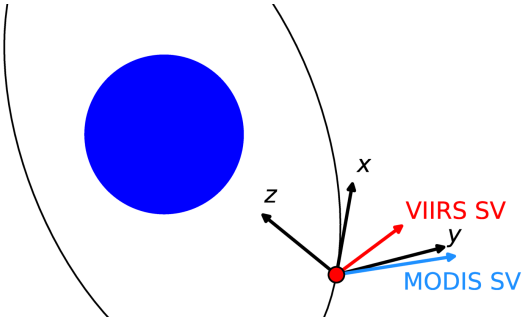

Fig. 2. Diagram of the instrument coordinate system for both MODIS and VIIRS, shown as x, y, and z. The MODIS SV vector is shown in blue in the yz-plane, at an angle of 8.425° from the y-axis away from z. The VIIRS SV vector is shown in red in the yz-plane, at an angle of 24.325° from the y-axis towards z.

as pointing towards nadir, with the x-axis perpendicular to z and pointing in the direction of orbital motion. The y-axis is defined as the cross product of z and x and is normal to the satellite orbital plane. This coordinate system can be seen in Figure 2. The scan mirror/RTA rotation is in the yz plane, and therefore the EV port and OBC/SV sectors will be located in this plane. In each scan, MODIS and VIIRS alternate views of the Earth with those of the OBCs and SV, from which the calibration and background data can be obtained, respectively. The MODIS SV port is located at 8.425° from the y-axis away from z and the VIIRS SV port is located at 24.325° from the y-axis towards z, as seen in Figure 2. For this work, we can further rotate the ICS in order to define an observation coordinate system, or OCS. Here, we rotate the ICS about x such that the y-axis is aligned with the SV port for each instrument. In practice, this coordinate system will be further rotated by the instrument roll angle during the observation, so that the y-axis points towards the Moon at the observation center time. We can use the SPICE toolkit developed by the Navigation and Ancillary Information Facility at NASA JPL along with the Developmental Ephemerides 430 (DE430) dataset in order to compute the Moon's position and relative orientation in the OCS, which will be discussed further in Section III [25], [26].

For radiometric calibration, the Moon is observed in a narrow phase angle range, approximately 1°, that is chosen based on the relevant instrument geometry (Terra views a waning Moon and Aqua, SNPP, N20 view a waxing Moon). In order to achieve this phase angle consistency between observations, each spacecraft uses a roll maneuver in order to align the SV port with the predicted position of the Moon at the time of the desired observation [9]. These observations require special mission planning and have been known in the literature as scheduled lunar observations. Table I shows several scheduled lunar observation parameters. Generally, lunar observations in the desired phase angle range are available for approximately 9 months in the calendar year. However, small changes to the relative orbits of the Moon and satellites over long time scales can change this availability. Unscheduled lunar observations, where the Moon happens to be visible through the SV port without a roll maneuver, occur in fewer months throughout the year but have more total observations, as the Moon can be seen for multiple orbits in a row over a wide range of phase angles.

TABLE I
MODIS AND VIIRS LUNAR OBSERVATION PARAMETERS. THE NUMBER OF OBSERVATIONS IS LISTED AS OF JANUARY 1, 2022.

Instrument	Launch Year	Phase Angle Range	Roll Angle Range	Number of Observations
Terra	1999	[55°, 56°]	[-20°, 0°]	213
Aqua	2002	[-56°, -55°]	[-20°, 0°]	200
SNPP	2011	[-51.5°, -50.5°]	[-14°, 0°]	84
N20	2017	[-51.5°, -50.5°]	[-14°, 0°]	33

For both MODIS and VIIRS during scheduled lunar observations, the EV data sector is rotated such that it overlaps the SV port in order to increase the total FOV compared to the nominal SV data sector. The FOV for both instruments in the EV sector is approximately ±55° in the scan direction. At scan angles far from nadir, the pixel size on ground increases, producing a distortion in the imagery known as the bow-tie effect [27]. While this is not compensated for in the MODIS imagery, for the VIIRS instrument, a pixel aggregation scheme was introduced in order to help mitigate this effect. The VIIRS raw pixel size for the I- and M-bands has an aspect ratio of three to one along-track to along-scan. For EV imagery at nadir, with no bow-tie effect, 3 along-scan samples are aggregated (3:1) in order to produce a pixel of equal size in both the scan and track directions. Away from nadir, the pixel size in the scan direction increases more compared to the track direction. At a scan angle of 31.7°, the sample aggregation is reduced to 2 (2:1) and 2 M-band (4 I-band) detectors are deleted in order to reduce scan-to-scan overlap in the imagery. At a scan angle of 44.9°, there is no aggregation (1:1) and 4 M-band (8 I-band) detectors are deleted.

For SNPP VIIRS, the sector rotation centers the EV sector on the SV, placing the Moon images at the center. However, for N20 VIIRS, the sector rotation places the SV near the edge of scan in order to capture more EV imagery during the lunar observation. This means that the N20 lunar image acquisition is in the 1:1 aggregation mode, and therefore appear elongated in the scan direction by a factor of 3, as shown in Figure 3. For N20 lunar observations, the detector deletion (known as bow-tie deletion) is also disabled. For SNPP, the pixel aggregation is performed on-board for most bands, and the Moon will appear circular in the images. However, for the dual gain M-bands (for RSB, M1-M5 and M7), the pixel aggregation is performed on ground, and therefore the Moon in these images will appear elongated like the N20 imagery, even when the Moon is at the nadir frame in the EV sector.

The MODIS and VIIRS imaging systems are also designed to create seamless EV imagery from scan-to-scan at nadir, with the instrument FOV and scan mirror/RTA rotation rate set to match the speed of the instrument ground track. However, the Moon is at a much greater distance from the satellites compared to Earth, and as a result, can be observed for multiple scans [10], [11]. The rate at which the Moon moves in the FOV of the sensor is determined by the geometry of

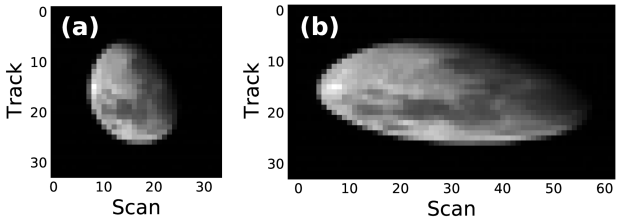

Fig. 3. Example lunar images from February 2018 for (a) SNPP VIIRS Band I1 and (b) N20 VIIRS Band I1. While both images are approximately the same size in the track direction, pixel aggregation makes the SNPP lunar image circular while the N20 images is approximately 3 times wider in the scan direction.

the observation, with the main component being the offset of the observation vector (SV location plus spacecraft roll angle) with the normal to the orbital plane (y-axis). Larger offsets from the y-axis will trace out a larger annulus on the celestial sphere and will, in general, observe the Moon for fewer scans. For observations of the full disk of the Moon, where the entire disk is visible on the FPA, all 4 instruments observed the Moon for a minimum of 5 scans across all scheduled Moon observations. However, since the VIIRS SV offset is larger and the maneuvering range is smaller (14° as compared to 20° for MODIS), the maximum number of full disk lunar observations is only 10 scans, compared to 18 scans for MODIS. Since extracting line profiles does not require the entire disk to be visible on the FPA, for the MTF calculations discussed in Section III, each data point will be calculated by combining all available line profiles (full disk or partial images) from each scheduled lunar observation. This greatly increases the amount of data available from each observation.

III. Methodology

The Moon has a long history of use in on-orbit spatial characterization of satellite instruments. The most widely implemented approach is to use the edge of the lunar disk to simulate a laboratory knife-edge measurement [20]. In recent years, this methodology has been extended to include a lunar surface variation correction for geostationary satellite imagers by Caron *et al.*, using a lunar albedo map from the Clementine mission.

For our work, the differences between our implementation of the lunar surface variation correction and the work in Caron *et al.* will be two-fold. The main difference relates to the low resolution images of the Moon acquired by the MODIS and VIIRS instruments compared to those of geostationary imagers, such as GOES ABI. At low resolution, a pixel interpolation approach was found to produce inconsistent model images because the scale of the surface variation in the lunar model is much less than the size of the pixel FOV on the lunar surface. Instead, we found that averaging the data for all of the model values that fell within the measured pixel's FOV produced better model data for low resolution images. In this section, we will detail the procedure used for accurately modeling the measured pixel footprint.

The second difference is related to the model used for the correction. For the Clementine data in Caron *et al.*, the albedo map produced was not specific to the observation geometry or the spectral response of the observation band. Since the Clementine reference is centered at 750 nm, an empirical spectral correction was derived using a simple photographic gamma function spectral albedo model. Using an iterative approach, the appropriate gamma values were derived for each of the channels through visual inspection of the images. For this work, we opt to use the SP model developed by the National Institute of Advanced Industrial Science and Technology (AIST) in Japan. With this model, we can input the known observation geometry to generate full lunar radiance maps over a range of wavelengths which can be weighted to match the spectral output of many of the MODIS and VIIRS bands. This output from the SP model accounts for differences in observation geometry across events, such as the lunar phase angle, which can impact the brightness across the visible lunar surface. In the following sections, we will discuss the implementation of this model in detail.

A. SP Model

The SELENE spacecraft was launched on September 14, 2007, and achieved orbit around the Moon on October 3, 2007 at an altitude of approximately 100 km from the surface [28]. SELENE contained 13 scientific instruments with primary objectives of studying the Moon's origin and evolution as well as performing a variety of measurements of the lunar surface environment. Among these instruments was the SP, which was able to measure the reflectance from the lunar surface in the wavelength range from 0.51 to 2.59 μm across 296 spectral channels [29]. The spectral channels are split into three groups, VIS (0.52 to 0.96 μm), NIR1 (0.88 to 1.68 μm), and NIR2 (1.70 to 2.59 μm). The SP resolution was 562 m along track and 400 m cross track, and obtained nearly continuous data from the lunar surface for approximately 7000 orbits, before the SELENE spacecraft entered a controlled descent to the lunar surface.

The SP measurements were developed into spatially-resolved models of the lunar surface first by Yokoto *et al.* and was further refined by Kouyama *et al.* in order to produce models at higher spatial resolution (0.5° compared to 1° in selenographic latitude and longitude) [24], [29], [30]. For this work, we use the model developed in Kouyama *et al.* with a tool provided to us by AIST in Japan, and will be referred to as the SP model throughout this work. The SP model output is mapped to 160 spectral channels from the VIS and NIR1 bands ranging in wavelength from 0.52 to 1.64 μm. Between 0.52 and 0.94 μm, the channels are separated by 6 nm, with the rest of the channels separated by 8 nm. The SP model takes six inputs in order to generate lunar radiance maps, with three related to the Sun's position and three related to the spacecraft position relative to the Moon. These positions are specified in terms of selenographic latitude and longitude (lunar coordinates) and the distance of each object from the Moon. For each lunar observation, the position of the spacecraft and Moon can be determined in the lunar coordinate system using the SPICE toolkit.

The output of the SP model is a GeoTIFF image with 160 layers corresponding to each of the output spectral channels.

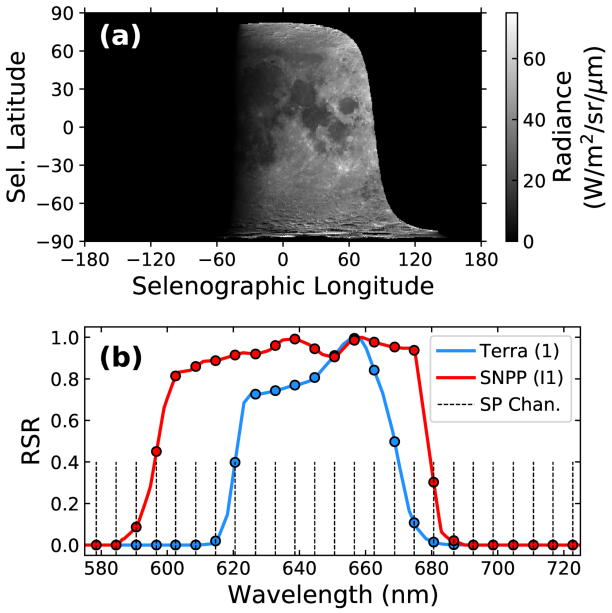

Fig. 4. (a) Example of the SP model output for the 638 nm channel for the SNPP VIIRS lunar observation on April 23, 2021. (b) Example projection of the SP model channel output onto the MODIS/VIIRS bands' RSR. The blue line shows the RSR for band 1 in Terra MODIS. The red line shows the RSR for band I1 in SNPP VIIRS. The black dotted lines show the location of the SP model channels in wavelength. The dots show relative weights given to each SP model channel for each band when creating the model maps.

Each layer is an image with 0.5° resolution in both selenographic latitude and longitude (720×360 pixels). An example image from an SP model channel can be seen in Figure 4(a). The next step after producing the model output is to create radiance maps specific to each band. This is done by taking the average of the SP model images for each channel weighted by the relative spectral response (RSR) for each MODIS or VIIRS band, as shown in Figure 4(b).

B. Creating Model Images

With the output from the SP model for each band, the next step is to project the map for each band onto the pixel locations of our measured images. This is done by first finding the location of the Moon in the measured image using a circular (or elliptical for some VIIRS bands) fit to the Moon edge. To find the Moon edge, we apply a Sobel filter to the measured image of the Moon, using the solar illumination angle to select only the lunar limb in the filter and to eliminate edges associated with the day/night terminator. The radius of the Moon image in pixel units, r, will be fixed based on the observation geometry and can be computed using the following equation:

$$r = \frac{R_M h}{d_M P} \tag{1}$$

where h, d_M, and P are the nominal altitude, spacecraft-Moon distance, and the nominal pixel size on ground at nadir. R_M is the radius of the Moon in km. For the dual gain M-bands in SNPP and for all of the N20 bands, the Moon will appear in the measured images with an aspect ratio of 3 since these bands have no sub-pixel aggregation (1:1), as discussed previously. For these bands, an elliptical fit is used.

With a known center location and size of the Moon in the image, the pixels are then mapped to selenographic latitude and longitude reference points. To facilitate this, we can defined a coordinate system for our measured images with axes x_m, y_m, and z_m, with the x_m-axis pointing out of the image plane, the y_m-axis in the scan direction, and the z_m-axis in the track direction. First, we assign each pixel corner a corresponding 3-dimensional vector of length r. For a given pixel corner location in the image, (i, j), where i is in the scan direction and j is in the track direction, the pixel corner vector can be written as:

$$\begin{aligned} z_m &= (j - z_{0,m}) \\ y_m &= -(i - y_{0,m})/a \\ x_m &= \sqrt{r^2 - y_m^2 - z_m^2} \end{aligned} \tag{2}$$

$y_{0,m}$ and $z_{0,m}$ are the measured center positions in the scan and track directions from the edge fit, respectively. a is the aspect ratio scaling factor, which is 1 for MODIS and the single gain bands in SNPP VIIRS, and 3 for N20 VIIRS and the SNPP VIIRS dual gain bands. In the pixel corner vectors, invalid values of the x_m component ($y_m^2 + z_m^2 > r^2$) imply a position that is off of the surface of the Moon. The next step is to rotate the vectors into the appropriate frame so they can be matched with the corresponding selenographic coordinates of the Moon. We first apply a rotation about x_m in order to align the lunar z-axis with z_m. The angle of this rotation can be computed based on the instrument orientation relative to the Moon in the OCS by projecting the lunar z-axis onto the imaging plane. In practice, we find that this angle can be optimized by minimizing the difference in radiance between the projected SP model image and measured image. Next, we apply rotations about y_m then z_m by the selenographic latitude and longitude of the observing instrument, respectively. These two rotations center the Moon coordinates at the proper location on the lunar surface.

By applying these rotations to the pixel corner vectors, we can convert the values from cartesian coordinates to selenographic latitude and longitude. Each pixel in the image will have 4 pixel vectors associated with each of the corners. If the value along the x_m-axis of each vector is invalid for all 4 pixel corners, this corresponds to a deep space pixel. If this value is valid for at least 1 pixel corner, and invalid for at least 1 other pixel corner, then this pixel corresponds to part of the lunar edge. If all 4 pixel corners are valid, then this corresponds to a lunar surface pixel. We keep a record of these designations to be used later in Section III-C.

To improve the shape of the pixel footprint on the lunar surface, we divide each pixel into 9 subpixels (3x3) and apply the mapping procedure outlined above. We then take the outer edges to represent the original pixel footprint. An example of this pixel projection is seen in Figure 5. In Figures 5(a) and (b), we show images from N20 VIIRS band I1 and Aqua MODIS band 1, respectively. In each image, we've highlighted the pixels around the Mare Crisium region of the lunar surface (3x3 for N20, 2x2 for Aqua). Using the mapping procedure

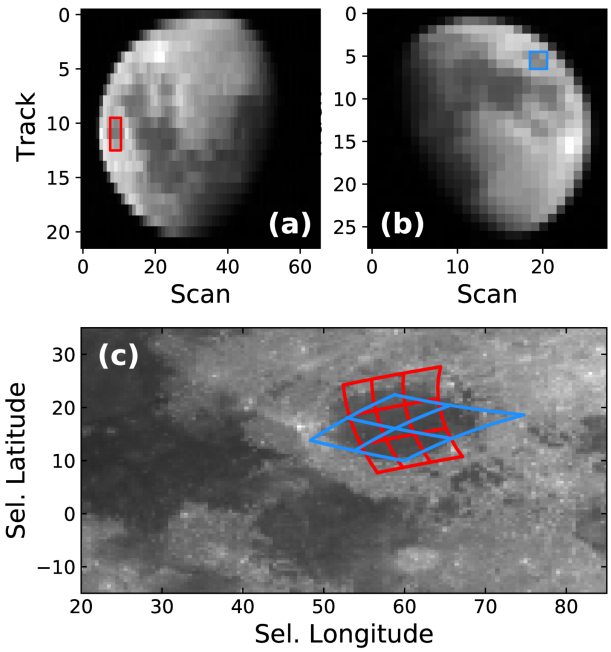

Fig. 5. Example projection of the instrument FOV on a map of the Moon's surface. (a) An example image from band I1 in N20 VIIRS, with the red box surrounding a 3x3 pixel ROI. (b) An example image from band 1 in Aqua MODIS, with the blue box surrounding a 2x2 pixel ROI. (c) A lunar map in an equirectangular projection. The FOV from each instrument in (a) and (b) is drawn on the surface in the corresponding colors.

outlined above, we can draw the pixel edges onto the SP model map in order to visualize the pixel footprint on the Moon. This can be seen in Figure 5(c). Here, we can see that since the two images are in different orientations and at different resolutions, the pixel footprints are not in alignment.

To create the model images used for the surface flattening correction, we take an average of the SP model radiance values on the surface that lie within a given pixels footprint. This is only done for pixels with all four corners on the lunar surface. An example of a measured and modeled image pair can be seen in Figure 6. To create a surface corrected image, both measured and modeled images can be normalized to their peak values and divided where valid surface pixels are present. This can be seen in Figure 6(c). Using this simple approach, we can see that the surface variation in the image is significantly reduced, particularly near the illuminated edge of the Moon from where we will extract our lunar profiles in the MTF calculation. This figure is just an example of the effectiveness of our image alignment and pixel projection procedure. For the profile extraction, a more sophisticated approach for surface flattening will be implemented for each line profile, and will be discussed in detail in Section III-C.

C. Deriving the Edge Spread Function

Using the model images derived above, we can now extract surface corrected line profiles from the data. The line profiles are obtained in both the scan and track directions from the illuminated portion of the lunar limb. The geometry of solar illumination on the image allows us to select the correct

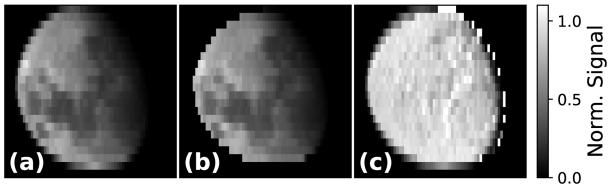

Fig. 6. Example of a simple lunar surface flattening correction. (a) A measured image of the lunar surface from N20 VIIRS band I1. (b) SP model output projected to the imager FOV (edge pixels removed). (c) Surface corrected image with edge pixel preservation.

profiles and avoid profiles that go over the day/night terminator instead of the lunar edge. In addition to these requirements, we prefer to extract line profiles from near the perpendicular edge of the Moon (with respect to the scan or track direction) to minimize the impact of the lunar curvature on the edge profile. To make this selection, we can use our space/edge/surface pixel designations described in the previous section. As the profiles get further from the center, a greater number of pixels along that line will have edge components. For this work, we will require that the line profiles contain no more that two edge pixels in order to stay closer to the center of the lunar disk. For example, for the image shown in Figure 6, 9 profiles would be selected from near the center of the image in the scan direction.

In Figure 7(a), we show an example of a single line profile extraction from Terra MODIS band 1 (blue circles). We also plot the model values over this data (black x's). For the measured data, the profile is first normalized to be 1 at the position of the last available surface pixel. The model data is then scaled using the ratio of the sum of the measured data divided by the sum of the modeled data over valid surface pixels. Finally, to produce the corrected profile, we divide the measured data by the modeled data at the location of the valid surface pixels. This has the effect of flattening the surface variation while preserving the edge, and is shown by the red circles.

A single profile will not be sufficient for deriving the edge spread function. Similar to previous work, data from multiple line profiles and multiple lunar images will be combined in order to create a smooth edge spread function [16], [18]–[23]. Since the lunar edge is curved and shifts position from scan-to-scan during a lunar observation event, the lunar disk edge will be sampled at slightly different locations, allowing us to achieve sub-pixel sampling of the edge position. By aligning all of the available line profiles, we will be able to gather data over the full range of the lunar edge. To accomplish this alignment, we fit the derivative of the corrected profiles to a gaussian curve in order to find the profile offset, as seen in Figure 7(b). We use the measured center position from each gaussian fit to apply offsets to each line profile for alignment. The results of this alignment can be seen in Figure 7(c). Here, we show both the uncorrected (blue) and corrected (red) data in order to highlight the effectiveness of the surface flattening correction.

At this point, we can more carefully consider the impact of the curved edge of the Moon on the profiles that we extract.

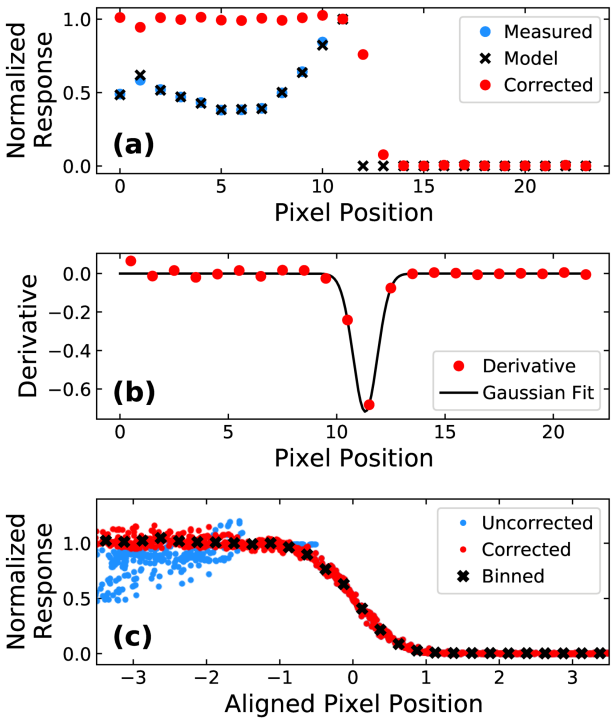

Fig. 7. Example correction and alignment of the edge profiles for the MTF calculation for Terra MODIS band 1 (a) A demonstration of a single profile correction. The modeled data (black x's) is used to remove the surface variation of the measured data (blue circles) to produce the surface corrected edge profiles (red circles). (b) The profile alignment for each edge profile is performed by using a Gaussian fit (black line) to the derivative of the surface corrected line profile (red circles). (c) The aligned profiles (red circles) can be binned into regions of 0.25 pixels and averaged (black x's). For comparison, the uncorrected profiles are also shown (blue circles).

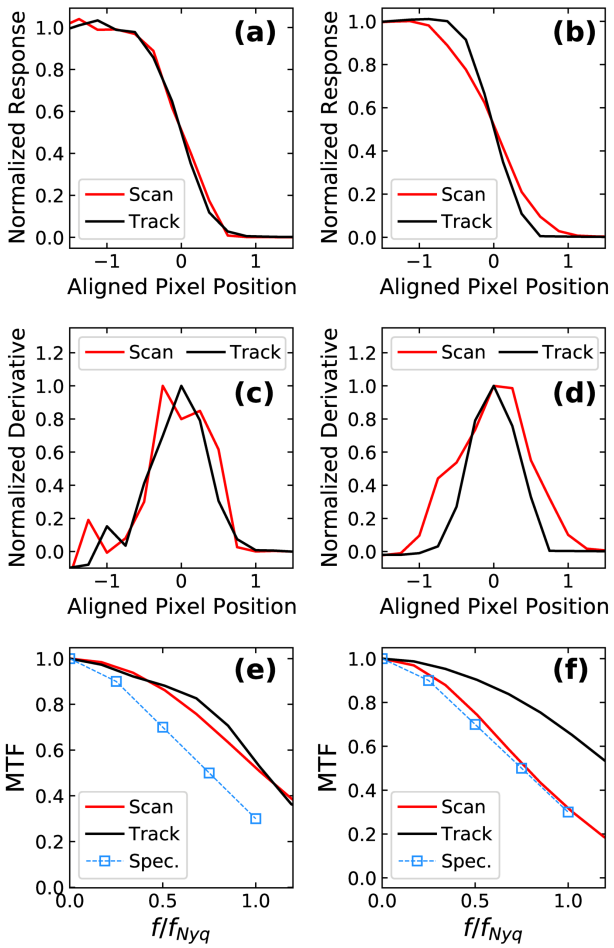

Fig. 8. An example of the MTF results derived from the aligned ESF data (left: SNPP; right: N20). (a) and (b) show the ESF data from band M10 in SNPP and N20 VIIRS, respectively, in both the scan and track directions. (c) and (d) show the derivatives (LSF) of the edge spread functions shown in (a) and (b), respectively. (e) and (f) show the MTF for the data shown in (c) and (d), respectively. The blue data in (e) and (f) show the MTF specifications for the VIIRS M-bands, which are the same for both the scan and track directions. The datasets for both instruments were collected on June 13, 2019.

As you take profiles away from the center of the Moon, the curvature of the Moon's disk angles the edge away from the perpendicular of the line scan. In work by Roland [31], it was found that the edge spread function could be corrected by multiplying the measured linewidth by the cosine of the angle between the edge normal and the direction from which the profile is obtained. In this work, we can apply this correction factor to the pixel positions after centering for each individual profile in order to account for the Moon's curvature.

To derive the MTF in the following section, we will need to have data at an even sampling rate. In Figure 7(c), the black x's represent the binned averages of the surface corrected data with a bin size of 0.25 pixels. At this bin size, we achieve sub-pixel resolution on the sampling while also ensuring that each bin has sufficient data for averaging. For the averaging, each point is weighted by the square of the curvature correction factor so that line profiles near the center of the Moon's disk are more heavily weighted. We also bin the values out to ± 6 pixels from the center position so that the FFT has a finer sampling interval. However, for images at lower resolution, this can cause fluctuations in the surface correction far away from the Moon edge which could adversely affect the MTF values [22], [23]. This is because the day/night terminator and lunar edge are separated by fewer pixels at lower resolution. To mitigate this, we replace the binned values that are more than ± 2.5 pixels from the edge with 0's and 1's for these bands.

We can compute the ESF in both the scan and track directions for each lunar observation, as shown in Figure 8(a) and (b) for SNPP and N20 band M10, respectively. For M10, SNPP scheduled lunar observations are aggregated in the scan direction (3:1 scan to track, aspect ratio of 1) as discussed previously whereas N20 is unaggregated (1:1 scan to track, aspect ratio of 3). In the SNPP data, the ESF profiles are nearly identical in the scan and track directions. However, for N20, we measure a slightly sharper response in the track direction compared to the scan direction owing to the difference in the pixel aspect ratio between the two images.

D. Calculation of the MTF

The MTF curves represent the response of the optical system to spatial changes and can be understood in the following way. A frequency of 0 represents the overall baseline signal of the image, and will generally be the peak of the FFT for

the images in this work. As we move to higher frequencies, higher values of the MTF at these frequencies means that the imager is able to resolve smaller spatial features. If our imager response was perfect, scanning over an ideal knife edge would produce an instantaneous change at the location of the edge for the ESF. The derivative of this ESF would produce a Dirac delta function for the line spread function (LSF). The Fourier transform of the Dirac delta function produces a flat line for the MTF values, meaning that the response at all spatial frequencies is equal. For real imaging systems, this is not the case, as the system resolution will limit the response at high spatial frequencies. Therefore, the MTF values generally decay as the spatial frequency increases.

In order to calculate the MTF from the ESF profiles derived in the previous section, we first compute the LSF by taking the derivative of the ESF data (then normalizing), as shown in Figure 8(c) and (d). Here, the width of the LSF is related to the sharpness of the response of the ESF. Again, for the N20 data, we see a difference in the width in the scan and track directions, with the track direction showing a sharper (narrower) response. Finally, the MTF curves are computed by taking the FFT of the LSF.

The MTF results for the LSF shown in Figure 8(c) and (d) are shown in Figure 8(e) and (f). The x-axis of these figures is scaled by the Nyquist frequency, f_{Nyq}, which is defined as half of the sampling rate, or 0.5 cycles per pixel. The MTF curves are also normalized at zero frequency. As was the case with the ESF and LSF data, the MTF curves for SNPP M10 are nearly the same in the scan and track directions. For N20, a sharper response in the track direction leads to a slower drop-off in the MTF values at increasing frequency. In these plots, we also show the MTF specifications at 0, 0.25, 0.5, 0.75, and 1.0 times the Nyquist frequency. These correspond to MTF values of 1.0, 0.9, 0.7, 0.5, and 0.3, respectively. The specifications are the same in the scan and track directions. Also, no separate specifications are given for different pixel aggregation modes. For MODIS, the MTF specifications are the same as those for VIIRS.

IV. Results and Discussion

With the methodology described in Section III, we derived the MTF using lunar measurements for each scheduled lunar observation for all 4 instruments in both the scan and track directions. The trending time series for select bands in each instrument can be seen in Figures 9−12. In these figures, we show the MTF values versus time at the Nyquist frequency. The MTF specification of 0.3 at the Nyquist frequency is also plotted as the black line.

For the MODIS data in Figures 9 and 10, we show the results for bands 1 (640 nm), 4 (555 nm), and 11 (531 nm), representing data for 250-m, 500-m, and 1-km resolution, respectively. These results are also summarized in Table II. For band 1 in both MODIS instruments, the MTF in the track direction is slightly higher than what is measured in the scan direction. A similar difference is also observed for band 4 in both instruments and band 11 in Aqua MODIS. Prelaunch measurements show a similar difference in the MTF in the

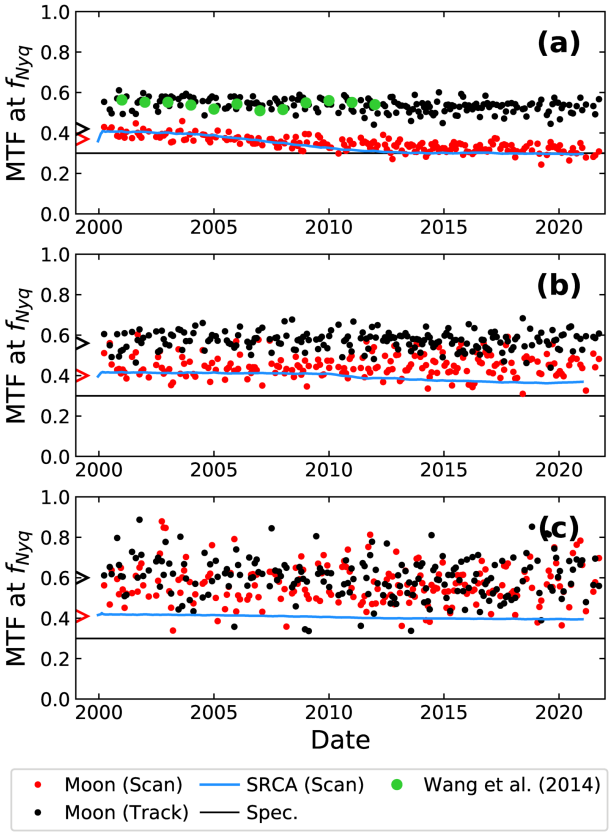

Fig. 9. Trending MTF for select bands in Terra MODIS: (a) band 1 (645 nm), (b) band 4 (555 nm), and (c) band 11 (531 nm). The red and black data points represent the MTF for each lunar observation in the scan and track directions, respectively. Red and black ">" symbols on the left side of the plot represent the pre-launch values. The black line shows the MTF specification (0.3). The blue line shows the MTF as measured by the SRCA in the scan direction. In (a), the green circles show the data as measured by Wang *et al.* for comparison [19]. All measurements and specifications are shown at the Nyquist Frequency.

track direction versus the scan direction, with each band in both instruments having a prelaunch MTF of approximately 0.4 in the scan direction, whereas the track MTF is closer to 0.6 for most bands (band 1 is lower at 0.42 for Terra and 0.49 for Aqua) [32]. The prelaunch values are shown in Figures 9−12 on the left side of each plot.

For band 1, the data in the scan direction shows a greater decay compared to the track direction over the course of the mission. Band 2 shows a similar decay in the MTF values in the scan direction as band 1, but is not shown in Figures 9 or 10. This trending has also been observed in previous measurements of the MODIS MTF [18], [19]. With the exception of the 250-m resolution bands (1 and 2) in the scan direction, the MODIS MTF values derived from the Moon in both directions are stable on orbit.

In the scan direction, we can compare our lunar MTF measurements to the MTF derived from the SRCA, as shown by the blue line in Figures 9 and 10 (the SRCA does not measure the MTF in the track direction). Here, we see good agreement between the lunar and SRCA results, particularly for band 1, with the SRCA data matching both the magnitude

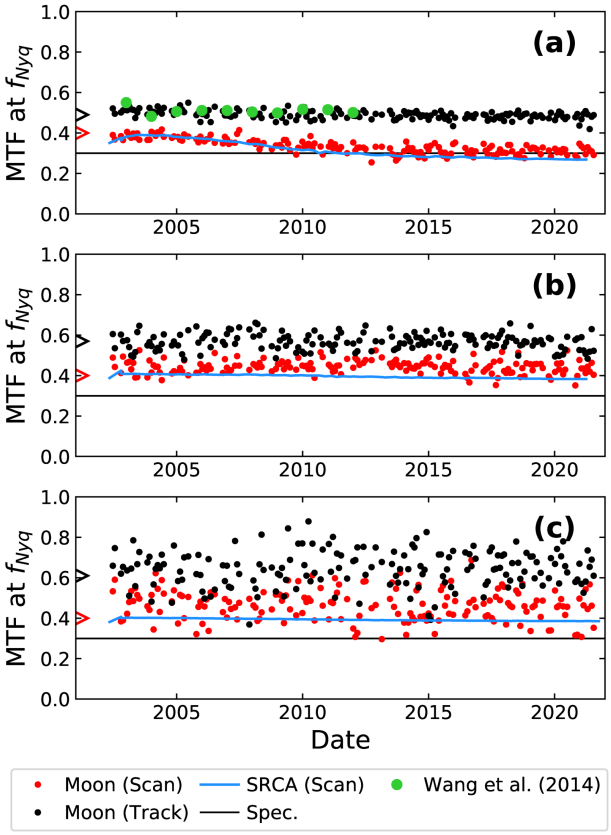

Fig. 10. Trending MTF for select bands in Aqua MODIS: (a) band 1 (645 nm), (b) band 4 (555 nm), and (c) band 11 (531 nm). The red and black data points represent the MTF for each lunar observation in the scan and track directions, respectively. Red and black ">" symbols on the left side of the plot represent the pre-launch values. The black line shows the MTF specification (0.3). The blue line shows the MTF as measured by the SRCA in the scan direction. In (a), the green circles show the data as measured by Wang *et al.* for comparison [19]. All measurements and specifications are shown at the Nyquist Frequency.

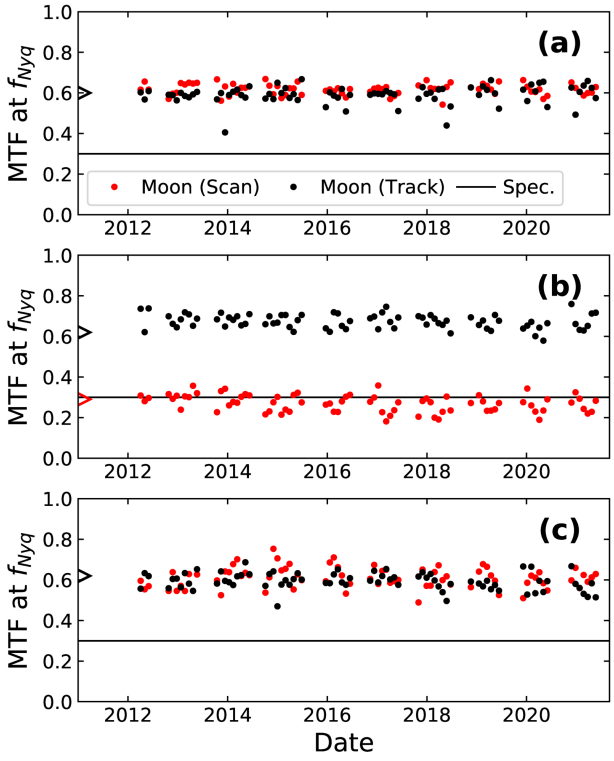

Fig. 11. Trending MTF for select bands in SNPP VIIRS: (a) band I1 (640 nm), (b) band M7 (865 nm), and (c) band M10 (1610 nm). The red and black data points represent the MTF for each lunar observation in the scan and track directions, respectively. Red and black ">" symbols on the left side of the plot represent the pre-launch values. The pre-launch values were specified for unaggregated data, therefore the results for I1 and M10 are not shown in the scan direction in this figure. The black line shows the MTF specification (0.3). All measurements and specifications are shown at the Nyquist Frequency.

and changes in the lunar MTF data throughout the mission. Also, as reported in previous work, the SRCA MTF measurements are scaled in order to match the MTF values derived during prelaunch testing [33]. Here, we apply the scale factors to the SRCA data, but no factors are applied to the lunar data. The agreement that we see between the SRCA and the Moon using the SRCA scale factors is similar to that observed in previous work using the Moon for MODIS [18], [19]. However, for band 11 in Terra MODIS, our MTF results in the scan direction are uniformly higher than those measured by the SRCA. This is not the case for Aqua MODIS where we have better agreement. Previous work using the Moon for the MTF did not include results for band 11 in the scan direction for comparison. At the time of this writing, the cause of this difference is still being investigated.

In other lunar-based MTF measurements by Wang *et al.*, the MTF is derived in both the scan and track directions for both MODIS instruments [19]. In the track direction, they provided a table of results for bands 1, 3, 8, and 10, of which only band 1 matches the spectral output of the SP model. In Figures 9 and 10, we plot the annual average results from Wang *et al.* in green for comparison (up to the year 2012). We see here that we are in very good agreement with the previously derived results. The variation of our data in the track direction is comparable for the 250-m and 500-m bands, but their data for the 1-km bands shows lower variation. This may point to an issue caused by improper alignment of the model images with the 1-km bands. Further refinement to this alignment will continue to be investigated. They also show results in the scan direction for band 1 in both instruments (tabulated results are not available) which shows a much greater variation when compared to our data, but with similar trends. For comparison of the MTF variation, we can look at the results in Figure 14 of Wang *et al.* over the first 1000 days. Their results show a min/max variation for Terra band 1 from approximately $0.34 - 0.55$ at the Nyquist frequency and from $0.29 - 0.47$ for Aqua. Our results over the same time period range from $0.38 - 0.45$ for Terra and $0.37 - 0.42$ for Aqua. In Figure 8 of Choi *et al.*, the results for Terra MODIS in the scan direction initially show a slightly larger variation compared Wang *et al.*, with a min/max variation of $0.26 - 0.58$ over the first 1000 days [18]. However, they use the angle of the Sun-Earth-Moon system in order to filter their data in order to reduce the level of noise while maintaining a similar trend, with a filtered min/max variation from $0.34 - 0.51$ shown in

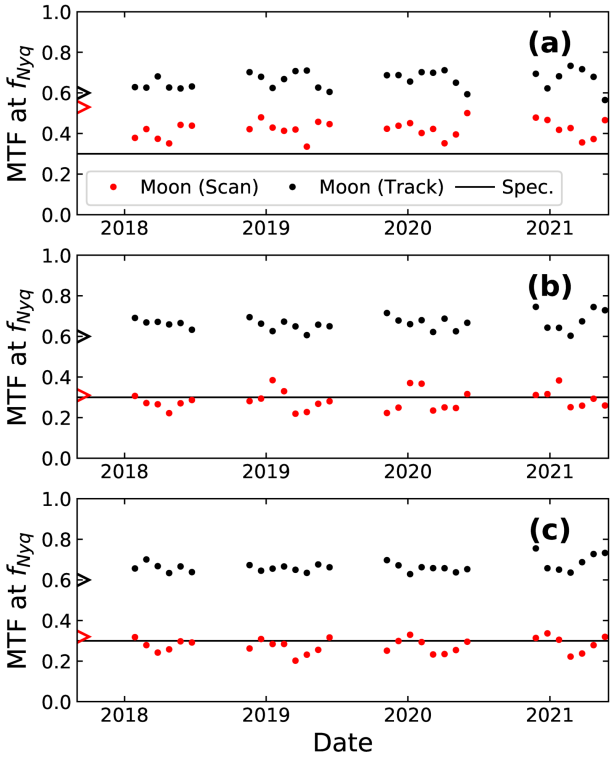

Fig. 12. Trending MTF for select bands in N20 VIIRS: (a) band I1 (640 nm), (b) band M7 (865 nm), and (c) band M10 (1610 nm). The red and black data points represent the MTF for each lunar observation in the scan and track directions, respectively. Red and black ">" symbols on the left side of the plot represent the pre-launch values. The black line shows the MTF specification (0.3). All measurements and specifications are shown at the Nyquist Frequency.

Figure 11 of Choi *et al.*. In our work, no event filtering is applied.

For the VIIRS data in Figures 11 and 12, we show the results for bands I1 (640 nm), M7 (865 nm), and M10 (1610 nm), representing data for the 375-m and dual and single gain 750-m bands, respectively. These results are also summarized in Table III. As seen before in the discussion of Figure 8, the bands with no pixel aggregation in the track direction show lower MTF values compared to the track direction. The aggregated bands show similar values in both directions. For SNPP VIIRS band I1 in the track direction, there are a few outlier data points which occur when the solar illumination angle is nearly perpendicular to the track direction. These observations provide the fewest number of line profiles to derive the MTF. For each band, the trend is stable throughout both missions.

Previous work using the Moon to derive the MTF for SNPP VIIRS showed the results in the track direction early in the mission [16], with values at the Nyquist frequency of approximately 0.6. Data for the scan direction was not shown. Similar to our work, the MTF values on orbit were stable. For our results, the unaggregated bands in SNPP match well with the previous work, whereas the data for the unaggregated band M7 is slightly higher with a mean value around 0.66. The N20 bands, which are also unaggregated, are also at around 0.66. Prelaunch measurements of the MTF for SNPP showed values of around 0.62 in the track direction for most of the M-bands [34], [35]. These prelaunch measurements also presented the results for the scan direction for unaggregated M-band pixels. For these bands, the results at the Nyquist frequency are all near the original specification of 0.3 but with some bands in SNPP below this threshold and some bands in N20 above the threshold. For our unaggregated data, the MTF values in the scan direction are also around the 0.3

TABLE II
MEASURED MTF IN THE SCAN AND TRACK DIRECTIONS FOR TERRA AND AQUA MODIS FOR SELECT BANDS AND YEARS. THE NUMBERS IN PARENTHESES REPRESENT THE STANDARD DEVIATIONS.

Instrument	Band	Year	MTF Scan	MTF Track
Terra	1	2000	0.409(21)	0.551(40)
		2005	0.381(17)	0.545(28)
		2010	0.334(23)	0.549(29)
		2015	0.327(20)	0.530(31)
		2020	0.311(27)	0.521(33)
	4	2000	0.466(57)	0.545(51)
		2005	0.452(56)	0.570(26)
		2010	0.442(36)	0.575(50)
		2015	0.455(55)	0.564(41)
		2020	0.447(35)	0.588(45)
	11	2000	0.571(70)	0.658(71)
		2005	0.531(128)	0.603(113)
		2010	0.603(88)	0.579(60)
		2015	0.539(63)	0.575(83)
		2020	0.592(150)	0.613(72)
Aqua	1	2002	0.376(12)	0.507(11)
		2005	0.373(13)	0.506(29)
		2010	0.337(25)	0.486(25)
		2015	0.311(27)	0.480(22)
		2020	0.308(20)	0.479(20)
	4	2002	0.459(60)	0.578(32)
		2005	0.429(25)	0.557(61)
		2010	0.451(38)	0.563(40)
		2015	0.447(23)	0.572(32)
		2020	0.435(47)	0.534(37)
	11	2002	0.474(103)	0.669(53)
		2005	0.445(72)	0.644(53)
		2010	0.497(64)	0.628(104)
		2015	0.460(84)	0.608(116)
		2020	0.441(72)	0.659(69)

TABLE III
MEASURED MTF IN THE SCAN AND TRACK DIRECTIONS FOR SNPP AND N20 VIIRS FOR SELECT BANDS AND YEARS. THE NUMBERS IN PARENTHESES REPRESENT THE STANDARD DEVIATIONS.

Instrument	Band	Year	MTF Scan	MTF Track
SNPP	I1	2012	0.609(28)	0.587(18)
		2015	0.609(27)	0.593(44)
		2020	0.611(25)	0.595(60)
	M7	2012	0.300(12)	0.683(48)
		2015	0.265(41)	0.672(35)
		2020	0.268(51)	0.654(53)
	M10	2012	0.575(36)	0.596(31)
		2015	0.621(43)	0.596(20)
		2020	0.605(34)	0.588(55)
N20	I1	2018	0.413(42)	0.649(32)
		2020	0.433(49)	0.666(43)
	M7	2018	0.274(25)	0.668(19)
		2020	0.301(52)	0.666(40)
	M10	2018	0.282(26)	0.660(22)
		2020	0.286(41)	0.663(39)

specification value. Our data also indicates that these values are stable on orbit, similar to the track direction.

While there are some small differences between our MTF results and the results of previous MTF measurements, the results are still in reasonable agreement for both instruments for both on-orbit and prelaunch measurements. The results from the MODIS scan direction also match well with the SRCA and previous lunar-based results, which gives us further confidence in the application of our technique. Also, for the results previously reported in the scan direction for MODIS, our technique reduces the level of variation significantly. However, for the 1-km bands, we see a higher variation which may point to limitations in our model image alignment.

V. Conclusions

In this work, we derived the mission MTF trending for select bands in MODIS and VIIRS using lunar observations. The Moon's edge was used in a similar manner as in slanted knife edge measurements in order to measure the system's spatial frequency response. In order to isolate the edge of the lunar limb in the ESF, the lunar surface variation was corrected using model images predicted by the SP model provided to us by AIST in Japan. We showed that by aligning the measured and modeled images, the MODIS and VIIRS pixels can be projected onto the SP model map in order to retrieve a co-registered model image of the Moon. Here, the surface variation of the Moon was corrected while the edge pixel response remained unaffected. This work shows that the surface variation correction works well for relatively low resolution images of the Moon as compared to the images from geostationary satellites in previous work.

We also compared the MTF trending results with previous work using the Moon, the SRCA (on MODIS), and prelaunch measurements. For both instruments, the results showed good agreement with the trends and stability derived in previous work. However, for the 1-km bands in MODIS, more investigation is needed into the alignment of the measured and modeled images, as the results here have more variability than previous works. For the scan direction in MODIS, our technique showed a significant improvement in the relative stability compared to the previously reported work.

In the future, the alignment of the SP model with measured imagery from MODIS and VIIRS can be used to perform a number of comparisons. One such investigation would be to use precise alignment of the model images in order to measure the spatial registration of the bands and detectors, which is important for co-registering EV images in the higher level MODIS and VIIRS science products. Further refinement of these alignment techniques would also likely yield improved results for the surface correction in the MTF calculations shown in this work, with improvements in the stability of the 1-km band results being desired. The SP model could also be used for radiometric gain tracking at select sites on the lunar surface. The results at different sites could be compared with each other and also with the results when using the ROLO model, which is currently in use for both MODIS and VIIRS [36].

Acknowledgment

The authors would like to thank Toru Kouyama of AIST for providing the tool used for creating the SP model images for our lunar observations. This tool was essential for this study and the code provided along with the documentation on its usage were greatly appreciated. We would also like to thank Daniel Link of SSAI for providing the MTF data from SRCA measurements in MODIS. We would also like to thank Yonghong Li and Amit Angal of SSAI along with our anonymous reviewers for reviewing this manuscript and providing valuable comments and suggestions.

References

[1] V. V. Salomonson, W. L. Barnes, X. Xiong, S. Kempler, and E. Masuoka, "An overview of Earth Observing System MODIS instrument and associated data systems performance," *Proc. IGARSS*, vol. 2, pp. 1174–1176, 2002.

[2] X. Xiong, J. Butler, K. Chiang, B. Efremova, J. Fulbright, N. Lei, J. McIntire, H. Oudrari, J. Sun, Z. Wang, and A. Wu, "VIIRS on-orbit calibration methodology and performance," *J. Geophys. Res. Atmos.*, vol. 119, pp. 5065–5078, 2014.

[3] C. Cao, F. Deluccia, X. Xiong, R. Wolfe, and F. Weng, "Early on-orbit performance of the Visible Infrared Imaging Radiometer Suite (VIIRS) onboard the Suomi National Polar-Orbiting Partnership (S-NPP) satellite," *IEEE Trans. Geosci. Rem. Sens.*, vol. 52, no. 2, pp. 1142–1156, 2014.

[4] X. Xiong, C. Cao, N. Lei, K. Chiang, A. Angal, Y. Li, S. Blonski, W. Wang, and T. Choi, "Early results from NOAA-20 (JPSS-1) VIIRS on-orbit calibration and characterization," *Proc. IGARSS*, vol. 2018, pp. 1112–1115, 2018.

[5] J. Sun, X. Xiong, A. Angal, H. Chen, A. Wu, and X. Geng, "Time-dependent response versus scan angle for MODIS reflective solar bands," *IEEE Trans. Geosci. Rem. Sens.*, vol. 52, no. 6, pp. 3159–3174, 2014.

[6] R. Bhatt, D. R. Doelling, A. Wu, X. Xiong, B. Scarino, C. O. Haney, and A. Gopalan, "Initial stability assessment of S-NPP VIIRS reflective solar band calibration using invariant desert and deep convective cloud targets," *Remote Sens.*, vol. 6, no. 4, pp. 2809–2826, 2014.

[7] S. Uprety, C. Cao, X. Xiong, S. Blonski, A. Wu, and X. Shao, "Radiometric intercomparison between Suomi-NPP VIIRS and Aqua MODIS reflective solar bands using simultaneous nadir overpass in the low latitudes," *J. Atmos. Ocean Tech.*, vol. 30, no. 12, p. 27202736, 2013.

[8] M. Bouvet, K. Thome, B. Berthelot, A. Bialek, J. Czapla-Myers, N. Fox, P. Goryl, P. Henry, L. Ma, S. Marcq, A. Meygret, B. Wenny, and E. Woolliams, "RadCalNet: A radiometric calibration network for earth observing imagers operating in the visible to shortwave infrared spectral range," *Remote Sens.*, vol. 11, no. 20, p. 2401, 2019.

[9] T. Wilson and X. Xiong, "Planning lunar observations for satellite missions in low-earth orbit," *J. Appl. Remote Sens.*, vol. 13, no. 2, p. 024513, 2019.

[10] J. Sun, X. Xiong, W. Barnes, and B. Guenther, "MODIS reflective solar bands on-orbit lunar calibration," *IEEE Trans. Geosci. Rem. Sens.*, vol. 45, no. 7, p. 2383, 2007.

[11] X. Xiong, J. Sun, J. Fulbright, Z. Wang, and J. Butler, "Lunar calibration and performance for S-NPP VIIRS reflective solar bands," *IEEE Trans. Geosci. Rem. Sens.*, vol. 54, no. 2, pp. 1052–1061, 2015.

[12] T. Choi, X. Shao, C. Cao, and F. Weng, "Radiometric stability monitoring of the suomi NPP visible infrared imaging radiometer suite (VIIRS) reflective solar bands using the moon," *Remote Sens.*, vol. 8, no. 1, p. 15, 2015.

[13] X. Xiong, J. Sun, S. Xiong, and W. L. Barnes, "Using the Moon for MODIS on-orbit spatial characterization," *Proc. SPIE*, vol. 5234, p. 480, 2004.

[14] X. Xiong, J. Sun, A. Angal, Y. Xie, T. Choi, and Z. Wang, "Results of MODIS band-to-band registration characterization using on-orbit lunar observations," *Proc. SPIE*, vol. 8153, pp. 81 531R–1, 2011.

[15] T. Wilson, A. Angal, and X. Xiong, "Orbital path and spacecraft attitude correction for the MODIS lunar spatial characterization," *IEEE Trans. Geosci. Remote Sens.*, vol. 52, no. 8, pp. 1063–1073, 2019.

[16] Z. Wang, X. Xiong, and Y. Li, "Update of VIIRS on-orbit spatial parameters characterized with the moon," *IEEE Trans. Geosci. Rem. Sens.*, vol. 53, no. 10, pp. 5486–5494, 2015.

[17] T. Choi, X. Shao, and C. Cao, "NOAA-20 visible infrared imaging radiometer suite (VIIRS) on-orbit band-to-band registration estimation for reflective solar band (RSB) using scheduled lunar collections," in *IGARSS 2019 - 2019 IEEE International Geoscience and Remote Sensing Symposium*, 2019, pp. 9059–9062.
[18] T. Choi, X. Xiong, and Z. Wang, "On-orbit lunar modulation transfer function measurements for the moderate resolution imaging spectroradiometer," *IEEE Trans. Geosci. Rem. Sens.*, vol. 52, no. 1, pp. 270–277, 2014.
[19] Z. Wang, X. Xiong, T. Choi, and D. Link, "On-orbit characterization of MODIS modulation transfer function using the moon," *IEEE Trans. Geosci. Remote Sens.*, vol. 52, no. 7, pp. 4112–4121, 2014.
[20] J. J. Shea, "Lunar limb knife-edge optical transfer function measurements," *Journal of Electronic Imaging*, vol. 8, no. 2, pp. 196–208, 1999.
[21] G. Keller, T. Chang, and X. Xiong, "MTF analysis using lunar observations for Himawari-8/AHI," *Proc. SPIE*, vol. 10402, pp. 104 022I–1, 2017.
[22] T. Wilson and X. Xiong, "Modulation transfer function characterization for GOES-16 advanced baseline imager using lunar observations," *Proc. SPIE*, vol. 11127, p. 111271Y, 2019.
[23] J. N. Caron and C. J. Rollins, "Improved lunar edge response function for on-orbit modulation transfer function calibration using albedo flattening," *J. Appl. Remote Sens.*, vol. 14, no. 3, p. 032408, 2020.
[24] T. Kouyama, Y. Yokota, Y. Ishihara, R. Nakamura, S. Yamamoto, and T. Matsunaga, "Development of an application scheme for the SELENE/SP lunar reflectance model for radiometric calibration of hyperspectral and multispectral sensors," *Planetary and Space Science*, vol. 124, pp. 76–83, 2016.
[25] C. H. Acton, "Ancillary data services of NASA's Navigation and Ancillary Information Facility," *Planetary and Space Sci.*, vol. 44, no. 1, pp. 65–70, 1996.
[26] W. Folkner, J. Williams, D. Boggs, R. Park, and P. Kuchynka, "The planetary and lunar ephemeris DE430 and DE431," *IPN Progress Reports*, vol. 42, no. 196, 2014.
[27] ATBD, VIIRS GEO, "Joint polar satellite system (JPSS) visible infrared imaging radiometer suite (VIIRS) geolocation algorithm theoretical basis document (ATBD)," 2013. [Online]. Available: https://www.star.nesdis.noaa.gov/jpss/Docs.php
[28] M. Kato, S. Sasaki, K. Tanaka, Y. Iijima, and Y. Takizawa, "The japanese lunar mission SELENE: Science goals and present status," *Adv. Space Res.*, vol. 42, no. 2, pp. 294–300, 2008.
[29] Y. Yokota *et al.*, "Lunar photometric properties at wavelengths 0.5 - 1.6 m acquired by SELENE Spectral Profiler and their dependency on local albedo and latitudinal zones," *Icarus*, vol. 215, no. 2, pp. 639–660, 2011.
[30] K. Ogohara, T. Kouyama, H. Yamamoto, N. Sato, M. Takagi, and T. Imamura, "Automated cloud tracking system for the Akatsuki Venus Climate Orbiter data," *Icarus*, vol. 217, no. 2, pp. 661–668, 2012.
[31] J. K. M. Roland, "A study of slanted-edge MTF stability and repeatability," *Proc. SPIE*, vol. 9396, p. 93960L, 2015.
[32] W. L. Barnes, T. S. Pagano, and V. V. Salomonson, "Prelaunch characteristics of the moderate resolution imaging spectroradiometer (MODIS) on EOS-AM1," *IEEE Trans. Geosci. Remote Sens.*, vol. 36, no. 4, pp. 1088–1100, 1998.
[33] T. Choi, N. Che, and X. Xiong, "On-orbit Aqua MODIS modulation transfer function trending in along-scan from the spectro-radiometric calibration assembly," *Proc. SPIE*, vol. 7081, p. 70810A, 2008.
[34] G. Lin, R. Wolfe, and M. Nishihama, "NPP VIIRS geometric performance status," *Proc. SPIE*, vol. 8153, p. 81531V, 2011.
[35] G. Lin and R. Wolfe, "JPSS-1 VIIRS at-launch geometric performance," *Proc. SPIE*, vol. 9972, p. 99721L, 2016.
[36] H. H. Kieffer and T. C. Stone, "The spectral irradiance of the Moon," *Astron. J.*, vol. 129, no. 6, pp. 2887–2901, 2005.

Truman Wilson received B.S. and Ph.D degrees in Physics from Colorado State University, Fort Collins, CO, USA, in 2007 and 2013, respectively.

He is currently a Lead Research Scientist for the MODIS Characterization Support Team and the VIIRS Characterization Support Team at Science Systems and Applications, Inc., Lanham, MD, USA.

Dr. Wilson was awarded a National Research Council Postdoctoral Fellowship at the National Institute of Standards and Technology, Gaithersburg, MD, USA, in 2013.

Xiaoxiong Xiong received the B.S. degree in optical engineering from the Beijing Institute of Technology, Beijing, China, and the Ph.D. degree in Physics from the University of Maryland at College Park, College Park, MD, USA.

He is an Optical Physicist at NASA/GSFC, Greenbelt, MD, USA, currently serving as the MODIS Project Scientist and the MODIS and VIIRS Calibration Scientist. In addition to remote sensing, he had also worked in the fields of optical instrumentation, nonlinear optics, laser/atomic spectroscopy, and mass spectrometry. See http://science.gsfc.nasa.gov/sed/bio/xiaoxiong.xiong-1 for more details.

Dr. Xiong is a fellow of SPIE.